CHEMISTRY OF MATERIALS
Article

Chem. Mater. **2010,** *22,* 1533–1539 1533
DOI:10.1021/cm902490g

Interconnected Networks of $Zn(NO_3)_2 \cdot 6(H_2O)$ Nanotubes and Its Solid-Phase Transformation into Porous Zinc Oxide Architectures

Ji Hong Wu,[†] Binni Varghese,[‡] Xue Dong Zhou,[†] Si Ying Teo,[†] Chorng Haur Sow,[‡] Siau Gek Ang,[†] and Guo Qin Xu*[,†]

[†]*Department of Chemistry, National University of Singapore, 3 Science Drive 3, Singapore 117543, Singapore and* [‡]*Department of Physics, National University of Singapore, 3 Science Drive 3, Singapore 117543, Singapore*

Received August 13, 2009. Revised Manuscript Received October 28, 2009

Highly oriented $Zn(NO_3)_2 \cdot 6H_2O$ nanotubes were grown on mica substrates based on an epitaxy mechanism. The $Zn(NO_3)_2 \cdot 6H_2O$ nanotubes with rectangular cross-section were self-assembled on mica surfaces into large-area, interconnected hexagonal networks. Fast evaporation of the solvent was found to be crucial for the growth of high-quality $Zn(NO_3)_2 \cdot 6H_2O$ rectangular nanotubes. ZnO architectures with tailored porosity were achieved through controlled solid-phase thermal decomposition of the $Zn(NO_3)_2 \cdot 6H_2O$ nanotubes. Defects in porous ZnO architectures and the photoluminescence (PL) properties could be well tuned by varying the annealing conditions. The porous ZnO interconnected networks were electrically interconnected and electrically functioned as a single integrated unit with symmetric, linear current−voltage ($I-V$) characteristic.

Introduction

It is widely recognized that the properties of nanomaterials depend not only on the composition and crystal structure and the size and shape but also on the way that they are organized into higher-order architectures. ZnO is an important wide band gap semiconducting material with interesting optical, optoelectronic, and piezoelectric properties. The optical properties of ZnO nanostructures largely depend on the size, shape, defects, and impurities [refs 1, 2, and references therein]. To achieve ZnO optical devices, it is important to realize the well-controlled structural properties as well as the light emissions by manipulating the fabrication of ZnO nanostructures. A variety of ZnO nanostructures have been reported, including nanoparticles,[3−5] nanorods,[6−8] nanowires,[9−11] nanobelts,[12−14] nanotubes,[15−18] core−shell structures,[19,20] and other complex hierarchical structures.[21,22] ZnO nanotubes, owing to the large surface area and possible quantum-confinement effect, have raised great interest recently.[23−27] A feasible strategy to further increase the surface area and hence to achieve enhanced functionality of ZnO nanotubes is the introduction of pores into their walls. However, such an attribute is rarely explored so far.[28,29] Current strategies toward highly porous structures include thermal decomposition,[30]

*To whom correspondence should be addressed. Fax: (65) 6779 1691. E-mail: chmxugq@nus.edu.sg.

(1) Djurišić, A. B.; Leung, Y. H. *Small* **2006**, *2*, 944.
(2) Özgür, Ü.; Alivov, Ya. I.; Liu, C.; Teke, A.; Reshchikov, M. A.; Doğan, S.; Avrutin, V.; Cho, S.-J.; Morkoç, H. *J. Appl. Phys.* **2005**, *98*, 041301.
(3) Beek, W. J. E.; Wienk, M. M.; Janssen, R. A. J. *Adv. Funct. Mater.* **2006**, *16*, 1112.
(4) Brayner, R.; Ferrari-Iliou, R.; Brivois, N.; Djediat, S.; Benedetti, M. F.; Fivet, F. *Nano Lett.* **2006**, *6*, 866.
(5) Kim, J. Y.; Osterloh, F. E. *J. Am. Chem. Soc.* **2005**, *127*, 10152.
(6) Kang, B. S.; Pearton, S. J.; Ren, F. *Appl. Phys. Lett.* **2007**, *90*, 083104.
(7) Wang, G.; Chen, D.; Zhang, H.; Zhang, J. Z.; Li, J. H. *J. Phys. Chem. C* **2008**, *112*, 8850.
(8) Wang, W.; Summers, C. J.; Wang, Z. L. *Nano Lett.* **2004**, *4*, 423.
(9) Xiang, B.; Wang, P.; Zhang, X.; Dayeh, S. A.; Aplin, D. P. R.; Soci, C.; Yu, D.; Wang, D. *Nano Lett.* **2007**, *7*, 323.
(10) Huang, M. H.; Samuel, M.; Feick, H.; Yan, H.; Wu, Y.; Kind, H.; Weber, E.; Russo, R.; Yang, P. *Science* **2001**, *292*, 1897.
(11) Nadarajah, A.; Word, R. C.; Meiss, J.; Konenkamp, R. *Nano. Lett.* **2008**, *8*, 534.
(12) Wang, W.; Zeng, B.; Yang, J.; Poudel, B.; Huang, J.; Naughton, M. J.; Ren, Z. *Adv. Mater.* **2006**, *18*, 3275.
(13) Kong, X. Y.; Wang, Z. L. *Nano Lett.* **2003**, *3*, 1625.
(14) Song, R.-Q.; Xu, A.-W.; Deng, B.; Li, Q.; Chen, G.-Y. *Adv. Funct. Mater.* **2007**, *17*, 296.
(15) Li, Q.; Kumar, V.; Li, Y.; Zhang, H.; Marks, T. J.; Chang, R. P. H. *Chem. Mater.* **2005**, *17*, 1001.
(16) Hu, J. Q.; Li, Q.; Meng, X. M.; Lee, C. S.; Lee, S. T. *Chem. Mater.* **2003**, *15*, 305.
(17) Sun, Y.; Fuge, G. M.; Fox, N. A.; Riley, D. J.; Ashfold, M. N. R. *Adv. Mater.* **2005**, *17*, 2477.
(18) Zhang, J.; Sun, L.; Liao, C.; Yan, C. *Chem. Commun.* **2002**, 262.
(19) Law, M.; Greene, L. E.; Radenovic, A.; Kuykendall, T.; Liphardt, J.; Yang, P. *J. Phys. Chem. B* **2006**, *110*, 22652.
(20) Haldar, K. K.; Sen, T.; Patra, A. *J. Phys. Chem. C* **2008**, *112*, 11650.
(21) Zhang, Y.; Xu, J.; Xiang, Q.; Li, H.; Pan, Q.; Xu, P. *J. Phys. Chem. C* **2009**, *113*, 3430.
(22) Lao, J. Y.; Wen, J. G.; Ren, Z. F. *Nano Lett.* **2002**, *2*, 1287.
(23) Li, L.; Pan, S.; Dou, X.; Zhu, Y.; Huang, X.; Yang, Y.; Li, G.; Zhang, L. *J. Phys. Chem. C* **2007**, *111*, 7288.
(24) Vayssieres, L.; Keis, K.; Hagfeldt, A.; Lindquist, S.-E. *Chem. Mater.* **2001**, *13*, 4395.
(25) Zhou, X. F.; Hu, Z. L.; Chen, Y.; Shang, H. Y. *Mater. Res. Bull.* **2008**, *43*, 2790.
(26) Jeong, J.-S.; Lee, J.-Y.; Cho, J.-H.; Suh, H.-J.; Lee, C.-J. *Chem. Mater.* **2005**, *17*, 2752.
(27) Li, M.-K.; Wang, D.-Z.; Ding, S.; Ding, Y.-W.; Liu, J.; Liu, Z.-B. *Appl. Surf. Sci.* **2007**, *253*, 4161.
(28) Wang, H.; Li, G.; Jia, L.; Wang, G.; Tang, C. *J. Phys. Chem. C* **2008**, *112*, 11738.
(29) Zhang, W.; Zhang, D.; Fan, T.; Ding, J.; Guo, Q. X.; Ogawa, H. *Nanotechnology* **2006**, *17*, 840.
(30) Yu, H.; Wang, D.; Han, M.-Y. *J. Am. Chem. Soc.* **2007**, *129*, 2333.

Published on Web 01/11/2010

chemical reduction,[31] Kirkendall counterdiffusion,[32] template-assisted methods,[33,34] etc. The thermal stability of zinc nitrate hexahydrate has drawn wide attention.[35−40] The releasing of gaseous side products during the thermal decomposition renders a promising way for the preparation of porous ZnO structures.

In the present study, we report the one-step synthesis of highly oriented, interconnected $Zn(NO_3)_2 \cdot 6H_2O$ nanotubes on mica substrates and subsequent solid-phase thermal decomposition into porous ZnO architectures. The $Zn(NO_3)_2 \cdot 6H_2O$ nanotubes with rectangular cross-section were prepared from a thin solution layer governed by an epitaxial growth mechanism. These epitaxial nanotubes were oriented along directions at ~60° to each other and self-assembled into large-area, interconnected hexagonal networks on mica surfaces. It was found that fast evaporation of the solvent was crucial for the formation of high-quality $Zn(NO_3)_2 \cdot 6H_2O$ rectangular nanotubes. While the overall geometrical configuration of the network-like assemblies was largely retained in the thermal decomposition of $Zn(NO_3)_2 \cdot 6H_2O$ nanotubes, the resulting porosity could be tailored by varying the annealing temperature and time. The photoluminescence (PL) spectra at room temperature (RT) exhibited a strong dependence on the annealing temperatures, implying that various types of defects were evolved in the porous ZnO architectures prepared at different temperatures. The electrical measurements demonstrated that the porous ZnO interconnected networks were electrically interconnected as a single integrated unit and exhibited a symmetric, linear current−voltage ($I-V$) characteristic.

Experimental Section

Zinc nitrate hexahydrate crystalline powder (reagent grade, 98%) was purchased from Aldrich and used as received. Solutions with concentrations in the range of 0.025−0.4 M were prepared by dissolving the zinc nitrate hexahydrate powder in Milli-Q water (Millipore, ≥18 $M\Omega \cdot cm^{-1}$). The mica substrate, $KAl_2(Si_3AlO_{10})(OH)_2$, was purchased from Mateck GmbH (http://www.Mateck.ed). Clean mica surface was prepared by cleaving in air prior to each sample preparation.

To grow $Zn(NO_3)_2 \cdot 6H_2O$ rectangular nanotubes, a droplet (~20 μL) of the zinc nitrate hexahydrate solution was pipetted onto a freshly cleaved mica surface and then removed quickly by N_2 gas flow. Such a process resulted in a thin solution layer on the mica surface, which was then subjected to rapid evaporation in N_2 atmosphere. After the N_2 gas flow was stopped, the mica slice was transferred into a desiccator and incubated for 1−3 h. To prepare porous ZnO architectures, the as-synthesized $Zn(NO_3)_2 \cdot 6H_2O$ nanotubes were annealed in a furnace (Barnstead Thermolyne, F4800 Furnace) at different temperatures for various lengths of time.

Morphology of the as-synthesized structures was characterized using scanning electron microscopy (SEM, JEOL JSM-5200) and field-emission SEM (FESEM, JEOL JSM-6701F). The crystallographic and composition information was obtained using powder X-ray diffraction (XRD, Siemens D5000, operated at 40 kV and 40 mA) with monochromatized Cu Kα radiation (λ = 1.54 Å), energy-dispersive X-ray spectroscopy (EDS, JSM-3010, operated at 300 kV), and selected area electron diffraction (SAED, JSM-3010, operated at 300 kV). The PL measurements were performed at RT using a He−Cd laser (325 nm) as the excitation source (Renishaw system 2000). The electrical properties were measured at RT in a FESEM chamber (JEOL, JSM7401-F, vacuum $< 10^{-4}$ Pa) equipped with nanomanipulators (sProber Nano-M, Zyvex Instruments). The piezo-controlled tungsten nanoprobes have a tip size typically < 50 nm.

Results and Discussion

1) Highly Oriented $Zn(NO_3)_2 \cdot 6H_2O$ Rectangular Nanotubes. Figure 1 shows typical SEM images of samples grown from a 0.1 M solution layer evaporated in N_2 atmosphere for ~20 s. The mica surface was covered with interconnected 1D nanostructures that were oriented in directions at ~60° to each other. These 1D nanostructures were self-assembled into isolated clusters (Figure 1A) or into extended networks (Figure 1C). A more careful and close-up view (Figure 1D) revealed that most of these 1D nanostructures have open rectangular ends, indicating the hollow tubular structure. More SEM characterizations of the tubular structure are described in the Supporting Information (Figure S1). When a lower concentration of 0.025 M was applied, isolated clusters were found to be the

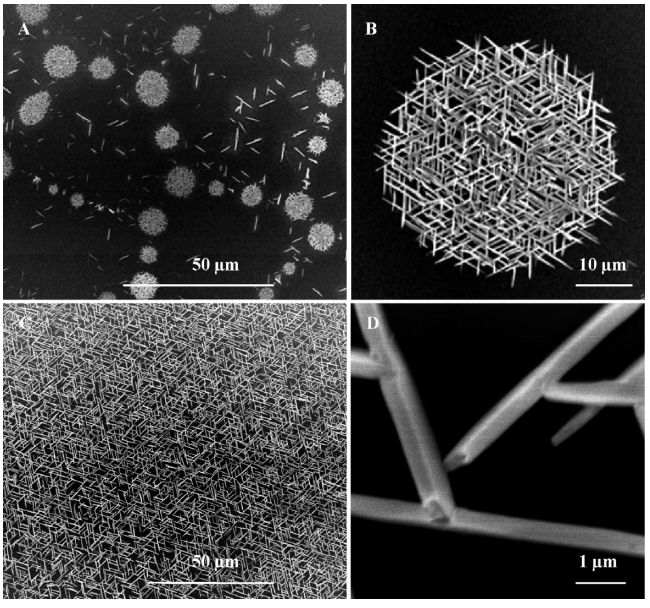

Figure 1. Highly oriented, interconnected $Zn(NO_3)_2 \cdot 6H_2O$ nanotubes on mica substrates, grown from a 0.1 M solution layer evaporated in N_2 atmosphere for ~20 s. (A) Nanotubes self-assembled in the form of isolated clusters. (B) Close-up view of a single cluster. (C) Nanotubes self-assembled in the form of extended networks. (D) Close-up views of (C).

(31) Yang, J.; Qi, L.; Lu, C.; Ma, J.; Cheng, H. *Angew. Chem., Int. Ed.* **2005**, *44*, 598.
(32) Navias, L. *J. Am. Ceram. Soc.* **1961**, *44*, 434.
(33) Lu, A. H.; Schüth, F. *Adv. Mater.* **2006**, *18*, 1793.
(34) Sun, D.; Riley, A. E.; Cadby, A. J.; Richman, E. K.; Korlann, S. D.; Tolbert, S. H. *Nature* **2006**, *441*, 1126.
(35) Shanmugam, Y.; Lin, F.-Y.; Chang, T.-H.; Yeh, C.-T. *J. Phys. Chem. B* **2003**, *107*, 1044.
(36) Jackson, J. G.; Novichikhin, A.; Fonseca, R. W.; Holcombe, J. A. *Spectrochim. Acta B* **1995**, *50*, 1423.
(37) Mu, J.; Perlmutter, D. D. *Thermochim. Acta* **1982**, *56*, 253.
(38) Małecki, A.; Małecka, B. *Thermochim. Acta* **2006**, *446*, 113.
(39) Kozak, A. J.; Wieczorek-Ciurowa, K.; Kozak, A. *J. Therm. Anal. Calorim.* **2003**, *74*, 497.
(40) Auffredic, J.-P.; Loür, D. *J. Solid State Chem.* **1983**, *46*, 245.

major product (Figure S2A), whereas extended networks were predominant at the concentration of 0.4 M (Figure S2B). The concentration-dependent self-assemblies can be explained as follows. During evaporation, the thin solution layer tends to rupture into small droplets to reduce the total free surface energy.[41] On the other hand, the $Zn(NO_3)_2 \cdot 6H_2O$ crystals appeared at the mica-solution interface serve as nails that can pin the solution layer against the mica surface and hence hinder it from rupture.[42] At higher concentration, the thin solution layer becomes saturated soon after the starting of evaporation. The $Zn(NO_3)_2 \cdot 6H_2O$ crystals emerge at the mica-solution interface before the solution layer ruptures, leading to the formation of large extended networks. On the contrary, when a low concentration (0.025 M) was applied, the thin solution layer was found to have ruptured into small isolated droplets before the occurrence of any noticeable crystallization at the mica-solution interface. Consequently, each small droplet developed into one isolated cluster.

Similar experiments were carried out on other substrates, including amorphous glass, Si(100), and highly ordered pyrolytic graphite (HOPG). Tubular crystals with random orientation were obtained on the surfaces of amorphous glass and Si(100) (Figure S3). However, no noticeable crystals were obtained on the surface of HOPG. This could be most likely due to the hydrophobic nature of the HOPG surface. It is probably that the N_2 gas flow completely removes the solution droplet from the HOPG surface. Consequently, thin solution layer is never formed on the HOPG surface, which is essential for the growth of $Zn(NO_3)_2 \cdot 6H_2O$ crystals. The hexagonal patterning on mica suggests a possible epitaxial growth mechanism, which is attributable to the surface lattice structure and ionic nature of mica. XRD results further suggests that the $Zn(NO_3)_2 \cdot 6H_2O$ nanotubes have {113} planes parallel to the mica substrate (as will be discussed later). Figure 2A and 2B shows the schematic models of the unit cell of orthorhombic $Zn(NO_3)_2 \cdot 6H_2O$ and its (113) plane, respectively. The atomic arrangement of the uppermost layer of cleaved mica is displayed in Figure 2C. Upon exposure to solution, K^+ cations at the uppermost layer will enter into the solution, leaving the vacancies (represented by the red dots in Figure 2D) available for the cation species in the solution. Figure 2D depicts the epitaxial alignment of $Zn(NO_3)_2 \cdot 6H_2O$ (113) plane at the cleaved mica surface. The $Zn(H_2O)_6^{2+}$ cations locate either at the vacancy sites or at the bridge sites (the middle sites between two neighboring red dots). The epitaxial orientations are $[010]_{mica} \parallel [1\bar{1}0]_{nitrate}$ and $[100]_{mica} \parallel [21\bar{1}]_{nitrate}$. The lattice mismatches along the directions of $[010]_{mica}$ and $[100]_{mica}$ are calculated to be -1 and 10%, respectively. The growth of 1D $Zn(NO_3)_2 \cdot 6H_2O$ nanotubes can be attributed to both its anisotropic orthorhombic structure[43] and the anisotropic lattice mismatches along two perpendicular directions.

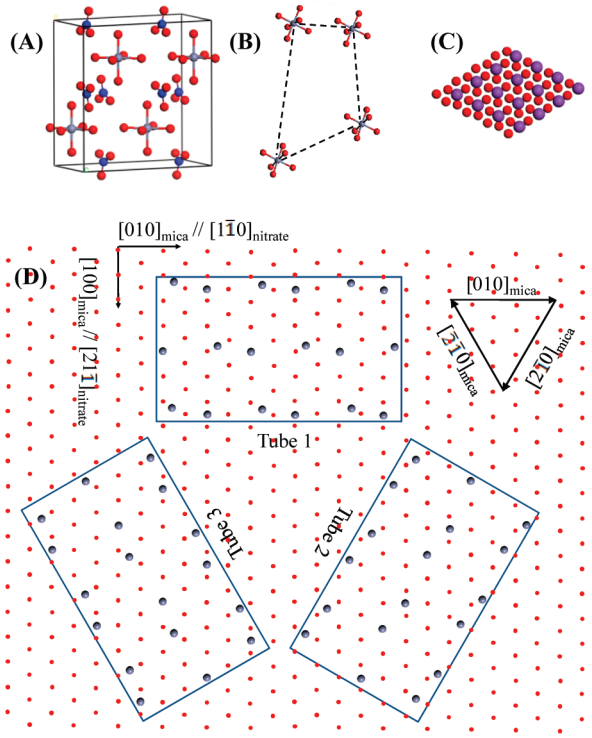

Figure 2. (A) Unit cell of orthorhombic $Zn(NO_3)_2 \cdot 6H_2O$. For clarity, H atoms of the water molecules are not shown. (B) (113) plane of $Zn(NO_3)_2 \cdot 6H_2O$. For clarity, NO_3^- anions are not shown. (C) Atomic arrangement of the uppermost layer of cleaved mica. (D) Schematical model illustrating the epitaxial alignment of the $Zn(NO_3)_2 \cdot 6H_2O$ (113) plane at the cleaved mica surface. For clarity, the water molecules coordinated with Zn^{2+} cations are not shown. Blue, red, grey, and purple balls represent N, O, Zn, and K atoms, respectively.

The nanotubes grow preferentially along the direction of $[010]_{mica}$ or $[1\bar{1}0]_{nitrate}$ (the direction with smaller lattice mismatch), whereas the growth is essentially hindered along the direction of $[100]_{mica}$ or $[21\bar{1}]_{nitrate}$ (the direction with larger lattice mismatch). Owing to the crystal symmetry of mica substrate, preferential growth can also take place along the identical directions of $[2\bar{1}0]_{mica}$ and $[\bar{2}10]_{mica}$. The nanotubes elongate until encounter each other or the complete depletion of $Zn(NO_3)_2 \cdot 6H_2O$ in solution, resulting in the formation of interconnected hexagonal networks.

The N_2-blowing time was found to be crucial for the nanotube growth. When the N_2 gas flow was cut off immediately after the solution droplet was removed from the mica surface, large thin-walled nanotubes with random orientation together with partially folded-up, randomly oriented small nanotubes were obtained (Figure S4). On the other hand, increasing the N_2-blowing time will yield more oriented small nanotubes (Figure 3). Due to large diameters and thin walls, most of the thin-walled nanotubes collapsed (Figures 3 and S4). Even though, their tubular structure can still be identified from the upward opening ends (denoted by the arrowheads, Figure 3B). The folding-up of these large collapsed nanotubes began either from one end of the large collapsed nanotube (Figure 3B, denoted by the arrows) or from its two long sides (Figure 3C). The folding-up were more complete with a longer N_2-blowing time

(41) Yabu, H.; Shimomura, M. *Adv. Funct. Mater.* **2005**, *15*, 575.
(42) Deegan, R. D.; Bakajin, O.; Dupont, T. F.; Huber, G.; Nagel, S. R.; Witten, T. A. *Nature* **1997**, *389*, 827.
(43) Xia, Y. N.; Yang, P.; Sun, Y. G.; Wu, Y. Y.; Mayers, B.; Gates, B.; Yin, Y. D.; Kim, F.; Yan, Y. Q. *Adv. Mater.* **2003**, *15*, 353.

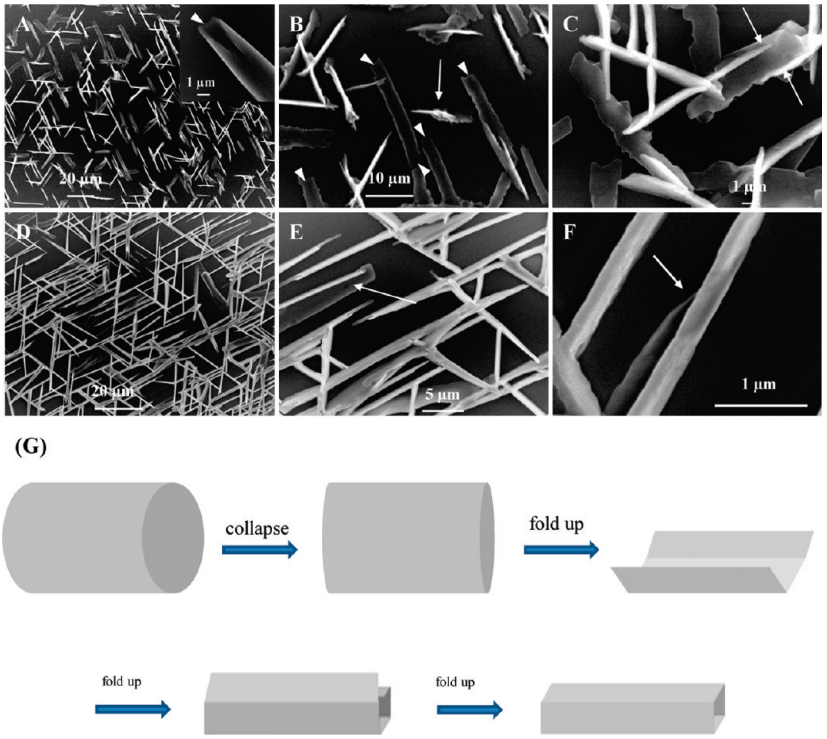

Figure 3. $Zn(NO_3)_2 \cdot 6H_2O$ nanotubes grown from a 0.4 M solution layer evaporated in N_2 atmosphere (A-C) for ~5 s and (D-F) for ~10 s. Inset of (A) shows a large thin-walled nanotubes. (G) Schematic model illustrating the folding-up of large thin-walled nanotube into small rectangular nanotube.

(Figure 3D-F). As discussed above, the oriented nanobutes were epitaxially grown on the mica substrate. The randomly oriented nanotubes shown in Figure S4, however, are nonepitaxial ones that crystallized at the solution-air interface and then deposited on the mica substrate. Figure S4 shows that some nonepitaxial nanotubes were folded up. Therefore, the folding-up behavior might be governed by some reason other than the lattice-mismatch-induced stress, which typically exists in the epitaxial crystals. Note that the thin solution layer was evaporated in two stages. First, it was rapidly evaporated in N_2 atmosphere. After the N_2 gas flow was stopped, the remaining solvent would be evaporated slowly in the desiccators. Therefore, a longer N_2-blowing time would lead to an overall faster crystal growth. The fast-grown nanotubes are of plenty of crystallographic defects. Stress originating from the crystallographic defects may be responsible for the folding-up phenomena. Figure 3G schametically illustrates the folding-up process beginning from the long sides of large collapsed nanotube.

2) Porous ZnO Architectures. The thermal transformation of $Zn(NO_3)_2 \cdot 6H_2O$ into ZnO begins at ~40 °C.[44] Intermediate hydrates of $Zn(OH)(NO_3) \cdot H_2O$ and $Zn_3(OH)_4(NO_3)_2$ as well as gaseous side products of the solid-phase transformation were reported in literature.[39,40] Curve (i) in Figure 4A shows the XRD pattern of bare mica. The $Zn(NO_3)_2 \cdot 6H_2O$ nanotubes grown on mica substrate presents a strong (113) reflection at 44.4° at RT (curve (ii), Figure 4A). The XRD results indicate that the as-synthesized $Zn(NO_3)_2 \cdot 6H_2O$ nanotubes were single-crystalline and with {113} planes (also the peripheral planes) parallel to the mica substrate. The small peak at 10.87° can be indexed to the (200) reflection of $Zn(NO_3)(OH) \cdot H_2O$ — one of the intermediate hydrates in the thermal decomposition of $Zn(NO_3)_2 \cdot 6H_2O$.[39] This indicates that a mild solid-phase transformation of $Zn(NO_3)_2 \cdot 6H_2O$ nanotubes readily took place at RT. The $Zn(NO_3)_2 \cdot 6H_2O$ nanotubes were then subjected to thermal annealing at 255 °C for various lengths of time. The evolution of XRD patterns were traced and shown in Figure 4A. The XRD pattern at 1 h (curve (iii)) shows reflections from the intermediate $Zn_3(OH)_4(NO_3)_2$ but with no reflection from $Zn(NO_3)_2 \cdot 6H_2O$, implying a completed conversion from $Zn(NO_3)_2 \cdot 6H_2O$ into $Zn_3(OH)_4(NO_3)_2$. The reflections of $Zn_3(OH)_4(NO_3)_2$ vanished at 4 h (Curve (iv)), indicating the end of thermal decomposition. On the other hand, the ZnO (002) reflection (hexagonal wurtzite, JCPDS card no. 36-1451) started to appear at 4 h, which was enhanced either by a prolonged annealing at the same temperature (Figure 4B) or by annealing at higher temperatures (Figure 4C).

Morphology evolution as a function of the annealing condition was monitored as well. Low-magnification SEM images (Figure S5) show that the overall geometrical configuration of the interconnected networks was largely retained after the high-temperature annealings. Close-up view revealed that nanosized pores began to be noticeable after annealing at 255 °C for 1 h, with small size and low density (Figure 5A). Both the pore size and density were greatly enhanced after annealing for another 3 h at the

(44) Małecki, A.; Małecka, B.; Gajerski, R.; Łabuś, S. *J. Therm. Anal. Calorim.* **2003**, *72*, 135.

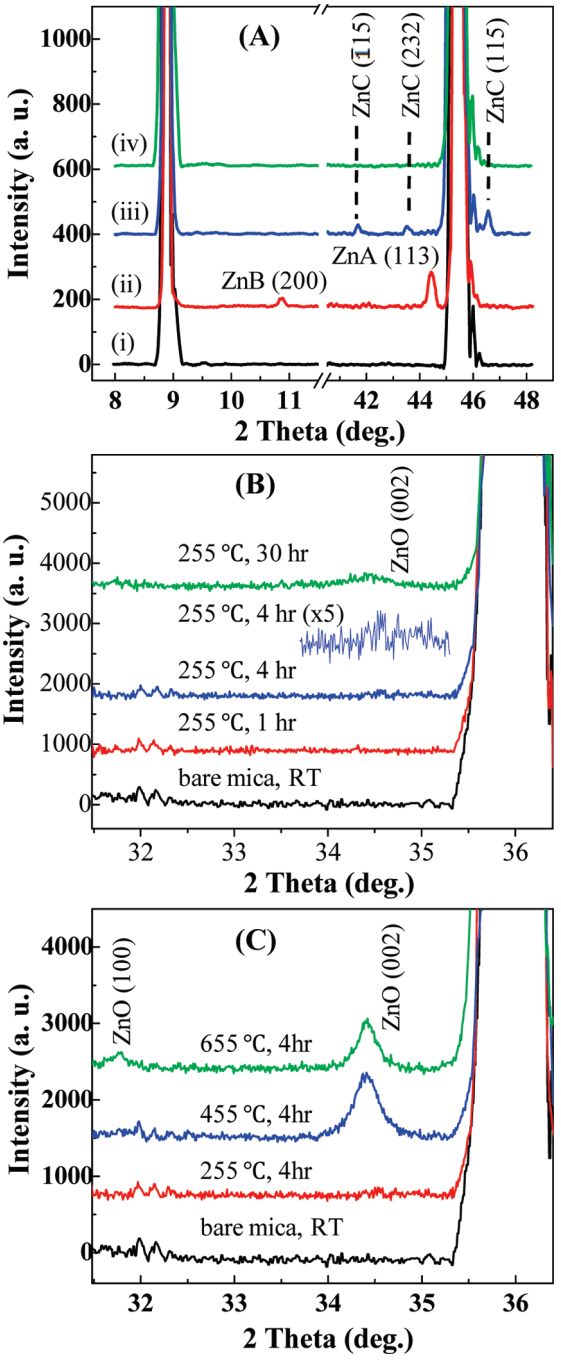

Figure 4. (A) Annealing time-dependent evolution of XRD patterns while annealing at 255 °C, recorded with a time-per-step parameter of 1 s: (i) bare mica; (ii) $Zn(NO_3)_2 \cdot 6H_2O$ nanotubes at RT; (iii) after annealing at 255 °C for 1 h; and (iv) after annealing at 255 °C for 4 h. ZnA, ZnB, and ZnC denote $Zn(NO_3)_2 \cdot 6H_2O$, $Zn(OH)(NO_3) \cdot H_2O$, and $Zn_3(OH)_4(NO_3)_2$, respectively. (B) Evolutions of ZnO XRD patterns as a function of the annealing time at 255 °C and (C) as a funtion of the annealing temperature, recorded with a time-per-step parameter of 20 s.

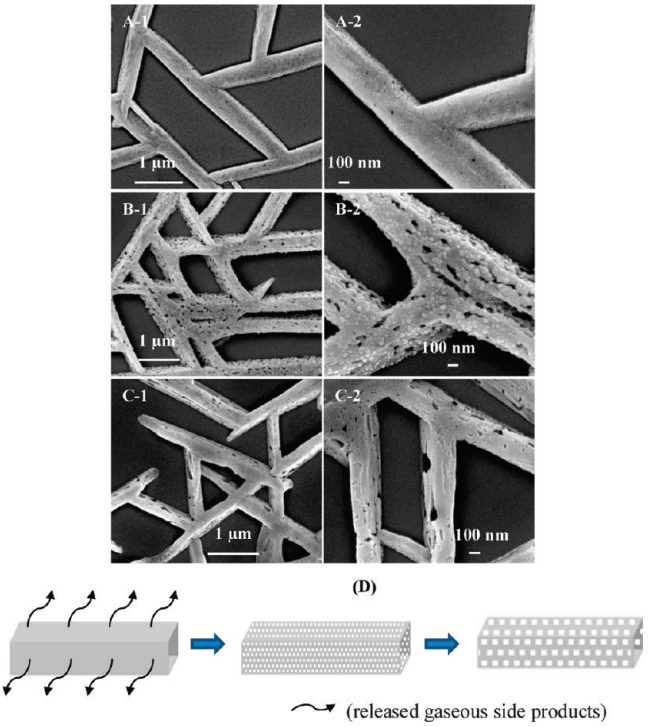

Figure 5. Annealing time-dependent morphology evolution of the porous ZnO architectures, after annealing at 255 °C for (A) 1 h, (B) 4 h, and (C) 30 h. The right panel is the close-up view of the left panel. (D) Schematic model illustrating the formation of pores in the nanotube walls as a result of releasing the gaseous side products.

same temperature (Figure 5B). When $Zn(NO_3)_2 \cdot 6H_2O$ nanotubes were subjected to high-temperature annealing, pores are supposed to form in the nanotube walls as a result of releasing the gaseous side products. On the other hand, pores might be formed due to the structural contraction from $Zn(NO_3)_2 \cdot 6H_2O$ (with density ~2.065 $g \cdot cm^{-3}$) to ZnO (with density ~5.606 $g \cdot cm^{-3}$) during the thermal annealing. Besides, the formation of pores might also be attributed to the self-organization and recrystallization of ZnO at high temperatures. After a long-term heating up to 30 h, the pore size was further increased, whereas the density dropped significantly (Figure 5C). This could be because the small pores have merged into larger ones, as schematically illustrated in Figure 5D. On the other hand, large pores could also be obtained by increasing the annealing temperature to 355 °C (Figure S6).

Nanosized ZnO granules started to appear at the temperature of 380 °C because of a rapid decomposition (Figure 6A). A close-up view disclosed that the ZnO granules formed at this temperature were still connected to each other (Figure 6A-2). Well-defined ZnO granules with an average size of ~20 nm were obtained at 430 °C. At the same time, the initial hollow tubular structure was replaced by an erect thin-ribbon structure (Figure 6B), which eventually fell on the mica substrate (Figure 6C). At higher temperatures, larger-sized ZnO granules were obtained as the small granules were melted and merged into larger ones. For example, the ZnO granules obtained at 655 °C had an average size of ~75 nm.

All the annealed samples exhibited two main PL emissions (Figure 7): the near-band-edge (NBE) excitonic related ultraviolet (UV) emission centered at ~380 nm, and the broad deep-level (DL) related visible emission in a wide range of 520−750 nm. Both UV and visible emissions show a strong dependence on the annealing temperature. With an increase in the annealing temperature, the intensity of UV emission was largely enhanced due to

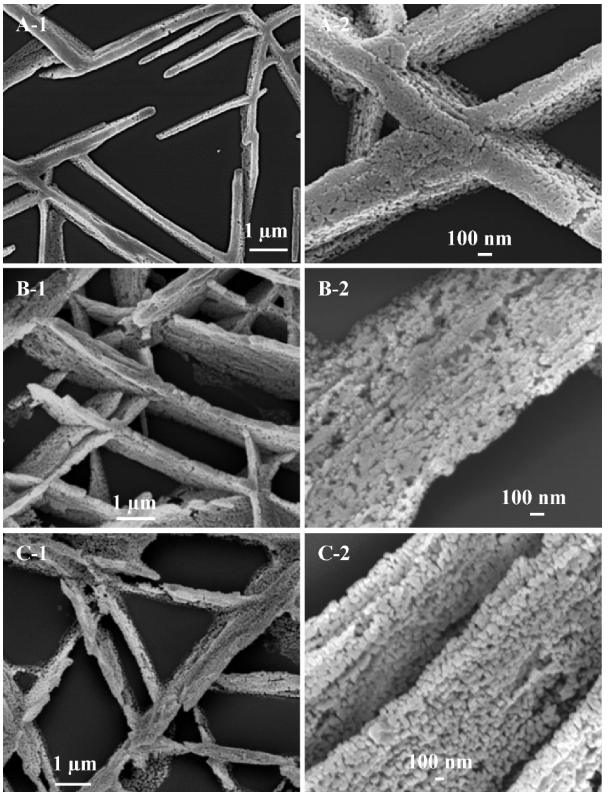

Figure 6. Nanosized ZnO granules after annealing 4 h at (A) 380 °C, (B) 430 °C, and (C) 655 °C. The right panel is the close-up view of the left panel.

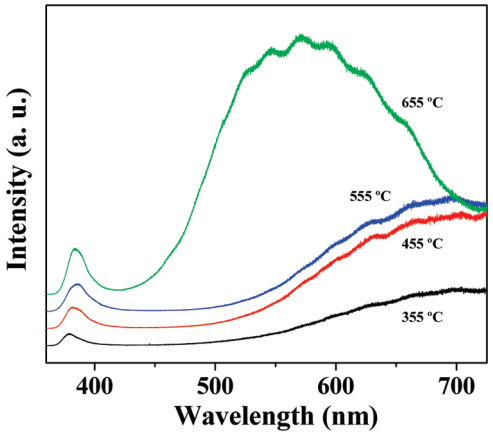

Figure 7. PL spectra of the porous ZnO architectures annealed at different temperatures.

an improved crystallinity of the ZnO samples.[45] The yellow-IR emissions can be attributed to the oxygen interstitials in the oxygen-rich ZnO,[46,47] which is also supported by the EDS analysis (Figure S7A). The 655 °C-annealed ZnO sample exhibited strong green-red emission. The largely enhanced intensity indicates the presence of large amount of defects.[48] An obvious blue shift of the visible emission was noticed as compared to the ZnO samples annealed at low temperatures. The green and yellow-red emissions are attributed to the oxygen vacancies and interstitials, respectively.[46−51] Generally, the green and yellow emissions cannot be observed simultaneously in the same sample.[52] In our case, the high-temperature annealing at 655 °C could possibly have broken the Zn−O bonds.[48] The ionized oxygen diffused out and resulted in the oxygen vacancies. The presence of oxygen vacancies in the high-temperature samples was also confirmed from the EDS spectrum (Figure S7B). Due to the short annealing time (4 h in this case), the oxygen vacancies (i.e., green defects) were limited in the surface layer with the interior oxygen interstitials (i.e., yellow-red defects) unmodified. As a result, broad green-red emission was achieved.

Electrical properties of the porous ZnO interconnected networks were examined using two-probe electrical measurements. Single porous ZnO architecture in the network assembly exhibited a symmetric, nonlinear $I-V$ response with a measured resistance (R_M) of ~0.74 MΩ (Figure 8A). The symmetric, nonlinear nature of the $I-V$ curve could either be due to the intrinsic semiconducting nature of the porous ZnO or be characteristic of the Schottky contact between the tungsten probe and the ZnO sample. As the distance between two probes was increased, a rise in the resistance and a transition from the nonlinear to linear $I-V$ response was observed (Figure 8B−C). The results indicate that the large interconnected network was electrically interconnected and functioned as a single integrated unit. In addition to the longer electrical path, the rise in resistance could be attributed to the large number of interfaces between the interconnected ZnO architectures. The linear $I-V$ characteristic could be due to the dominant contribution from the interconnected ZnO architectures compared to that from the Schottky contacts. We have also studied the electrical properties of the isolated clusters with different sizes (Figure S8). Similar to the extended network, the clusters showed a symmetric, linear $I-V$ response. We have measured the conductivity of the porous ZnO interconnected networks under UV irradiation. The conductivity of the ZnO networks was largely enhanced due to the UV irradiation. The conductivity of ZnO can also be modified by the adsorption of gases, such as CO.[53] NH_3[54] Further investigations on the possible applications

(45) Cho, S.; Ma, J.; Kim, Y.; Sun, Y.; Wang, G.; Ketterson, J. B. *Appl. Phys. Lett.* **1999**, *75*, 2761.
(46) Greene, L. E.; Law, M.; Goldberger, J.; Kim, F.; Johnson, J. C.; Zhang, Y.; Saykally, R. J.; Yang, P. *Angew. Chem., Int. Ed.* **2003**, *42*, 3031.
(47) Li, D.; Leung, Y. H.; Djurišić, A. B.; Liu, Z. T.; Xie, M. H.; Shi, S. L.; Xu, S. J.; Chan, W. K. *Appl. Phys. Lett.* **2004**, *85*, 1601.
(48) Zhong, J.; Kitai, A. H.; Mascher, P. *J. Electrochem. Soc.* **1993**, *140*, 3644.
(49) Vanheusden, K.; Warren, W. L.; Seager, C. H.; Tallant, D. R.; Voigt, J. A.; Gnade, B. E. *J. Appl. Phys.* **1996**, *79*, 7983.
(50) Vanheusden, K.; Seager, C. H.; Warren, W. L.; Tallant, D. R.; Voigt, J. A. *Appl. Phys. Lett.* **1996**, *68*, 403.
(51) Li, Y.; Meng, G. W.; Zhang, L. D.; Phillipp, F. *Appl. Phys. Lett.* **2000**, *76*, 2011.
(52) Studenikin, S. A.; Golego, N.; Cocivera, M. *J. Appl. Phys.* **1998**, *84*, 2287.
(53) Ryu, H.-W.; Park, B.-S.; Akbar, S. A.; Lee, W.-S.; Honga, K.-J.; Seo, Y.-J.; Shin, D.-C.; Park, J.-S.; Choi, G.-P. *Sens. Actuators, B* **2003**, *96*, 717.
(54) Law, J. B. K.; Thong, J. T. L. *Nanotechnology* **2008**, *19*, 205502.

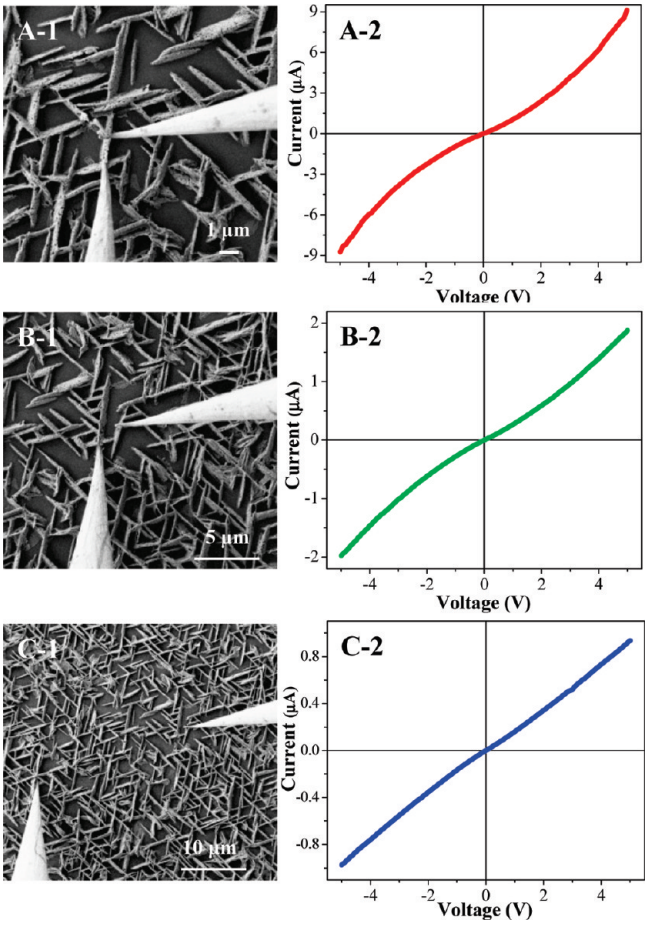

Figure 8. Electrical properties of the porous ZnO interconnected networks as a function of the distance between two tungsten probes: (A) $R_M \sim 0.74$ MΩ, (B) $R_M \sim 3.21$ MΩ, and (C) $R_M \sim 6.0$ MΩ.

of the porous ZnO interconnected networks in photo and gas-sensing will be explored.

Conclusions

In conclusion, the epitaxial growth of $Zn(NO_3)_2 \cdot 6H_2O$ rectangular nanotubes on mica substrates was demonstrated. The solid-phase thermal transformation of $Zn(NO_3)_2 \cdot 6H_2O$ nanotubes into porous ZnO architectures was explored. The epitaxial $Zn(NO_3)_2 \cdot 6H_2O$ nanotubes were oriented in directions at approximately 60° to each other and self-assembled into large-area, interconnected hexagonal networks. The ZnO architectures with well-tailored porosities were fabricated through the solid-phase thermal decomposition of $Zn(NO_3)_2 \cdot 6H_2O$ nanotubes under different annealing conditions. The PL spectra exhibited a strong dependence on the annealing temperatures, suggesting the presence of various types of defects in the porous ZnO architectures annealed at different temperatures. The porous ZnO interconnected networks were electrically interconnected and functioned as a single integrated unit that exhibited a symmetric, linear $I-V$ characteristic. The epitaxial growth together with the folding-up phenomena renders an intelligent approach to synthesize oriented tubular structures. The synthesis approach described in this article could be further explored to synthesize other 1D materials with unique structures and properties.

Acknowledgment. We acknowledge the financial support from the Ministry of Education, Singapore, Grant No. R-143-000-250-377. Ji Hong Wu also acknowledges the award of graduate scholarship from National University of Singapore.

Supporting Information Available: High-resolution SEM characterizations of the tubular structures, $Zn(NO_3)_2 \cdot 6H_2O$ nanotubes grown on amorphous glass and Si(100), EDS analysis of the low-temperature and high-temperature ZnO samples, and electrical conductivity of isolated ZnO clusters. This material is available free of charge via the Internet at http://pubs.acs.org.